Faraday Discussions

Cite this: *Faraday Discuss.*, 2018, **206**, 159

PAPER

View Article Online
View Journal | View Issue

Design principles from multiscale simulations to predict nanostructure in self-assembling ionic liquids†

Benjamin T. Nebgen,‡*[ab] Harsha D. Magurudeniya,‡[a]
Kevin W. C. Kwock,§[a] Bryan S. Ringstrand,[a] Towfiq Ahmed,[b]
Sönke Seifert,[c] Jian-Xin Zhu,[ab] Sergei Tretiak[ab]
and Millicent A. Firestone *[a]

Received 29th April 2017, Accepted 18th July 2017
DOI: 10.1039/c7fd00154a

Molecular dynamics simulations (up to the nanoscale) were performed on the 3-methyl-1-pentylimidazolium ionic liquid cation paired with three anions; chloride, nitrate, and thiocyanate as aqueous mixtures, using the effective fragment potential (EFP) method, a computationally inexpensive way of modeling intermolecular interactions. The simulations provided insight (preferred geometries, radial distribution functions and theoretical proton NMR resonances) into the interactions within the ionic domain and are validated against ^{1}H NMR spectroscopy and small- and wide-angle X-ray scattering experiments on 1-decyl-3-methylimidazolium. Ionic liquids containing thiocyanate typically resist gelation and form poorly ordered lamellar structures upon mixing with water. Conversely, chloride, a strongly coordinating anion, normally forms strong physical gels and produces well-ordered nanostructures adopting a variety of structural motifs over a very wide range of water compositions. Nitrate is intermediate in character, whereby upon dispersal in water it displays a range of viscosities and self-assembles into nanostructures with considerable variability in the fidelity of ordering and symmetry, as a function of water content in the binary mixtures. The observed

---

[a] *Materials Physics & Applications, Center for Integrated Nanotechnologies, Los Alamos National Laboratory, P.O. Box 1663, Los Alamos, NM, USA 87545. E-mail: firestone@lanl.gov; bnebgen@lanl.gov; Tel: +1-505-695-8837*

[b] *Theoretical Division, Center for Integrated Nanotechnologies, Los Alamos National Laboratory, P.O. Box 1663, Los Alamos, NM, USA 87545. Tel: +1-505-697-0924*

[c] *X-ray Sciences Division, Argonne National Laboratory, Lemont, IL, USA 60439*

† Electronic supplementary information (ESI) available: Comparison of force field parameters, mean squared displacement *vs.* time for MD simulations, simulated and experimental water self-diffusion coefficients, ^{1}H and ^{13}C spectra of $C_{10}mim^+A^-$, where $A^- = NO_3^-$, SCN^-, Br^-. TGA scans of $C_{10}mim^+A^-$, where $A^- = Cl^-$, NO_3^-, SCN^-. DSC scans of $C_{10}mim^+A^-$, where $A^- = NO_3^-$, SCN^-. FT-IR spectra of $C_{10}mim^+A^-$, where $A^- = Cl^-$, NO_3^-, SCN^-. See DOI: 10.1039/c7fd00154a

‡ These authors contributed equally to the work.

§ Kevin W. C. Kwock is an undergraduate research participate from Case Western Reserve University, Cleveland OH.

changes in the macro and nanoscale characteristics were directly correlated to ionic domain structures and intermolecular interactions as theoretically predicted by the analysis of MD trajectories and calculated RDFs. Specifically, both chloride and nitrate are positioned in the plane of the cation. Anion to cation proximity is dependent on water content. Thiocyanate is more susceptible to water insertion into the second solvent shell. Experimental ^{1}H NMR chemical shifts monitor the site-specific competition dependence with water content in the binary mixtures. Thiocyanate preferentially sits above and below the aromatic ring plane, a state disallowing interaction with the protons on the imidazolium ring.

Introduction

There are significant on-going research efforts in devising amphiphile systems that predictably self-assemble into nanostructures to produce materials for directional (ionic, electronic or molecular) transport, structured reaction media, or scaffolding for the integrative assembly of multiple nanoconstituents.[1–4] These materials, however, have yet to achieve the fidelity and complexity in functional structures found in self-assembled soft matter that exists in nature, such as proteins, biomembranes, and viral capsids.[4,5] The elaborate structures and functions found in natural soft matter biosystems provides the motivation for improving wholly synthetic molecular constituents designed to autonomously organize into well-defined architectures that adopt a wide spectrum of structural motifs. In spite of the collective efforts in self-assembly, the design rules for selection of the resultant nanoscale structure and prediction of physical properties remain lacking. Continued opportunities exist for advancing our fundamental understanding of the relationship between the molecules and the resulting nanostructure created. Central to this endeavour is theoretical modelling coupled with experiments to advance our understanding of requisite information (shape, chemical moieties, *etc.*) to be encoded in the primary molecular amphiphiles, here specifically 1,3-dialkylimidazolium ionic liquids, for reliable and predictable generation of self-assembled nanostructures upon dispersal in water.

Previously, we noted that the molecular structure of many room temperature ionic liquids (ILs) resembles conventional cationic surfactants, and therefore they could be self-assembled into non-covalent nanostructures in water.[6,7] The self-assembling systems initially studied were composed of binary mixtures of water and 1-decyl-3-methylimidazolium IL cations paired with halides or nitrate.[6,7] In general, the formed lyotropic mesophases were strong physical gels, adopting a wide variety of structural motifs including 1-D lamellar, 2-D hexagonal, 3-D cubic phases, and hybrid constructions, such as hexagonal or tetragonal modulated and perforated lamellae.[6,7] These early studies spawned the exploration of ILs containing polymerizable groups (*i.e.*, IL monomers) similarly self-assembled in water and then polymerized to yield durable, solvent responsive nanostructured materials.[8–11] It was observed that introducing certain polymerizable groups or changing the substitution pattern of moieties on the IL cation, and/or changing the anion, dramatically altered the architectures produced by self-assembly.[7,12] Concurrent studies carried out on binary mixtures of ILs and water,[13] and numerous studies evaluating the inherent structural heterogeneity in neat ILs and IL/organic solvent mixtures (*e.g.*, short chain alcohols, hexane, *etc.*), have been conducted; yet they do not resolve the question of how molecular IL structure yields a particular nanostructure.[14–19] Despite a considerable amount of research activity on this topic, the rational, *a priori* design of self-assembled nanostructured IL based materials remains elusive. The current state of knowledge within the IL community has been recently reviewed.[20] This lack of understanding may be attributed to experiments that fail to fully evaluate the multi-length scale non-covalent interactions in relation to the nanoscale self-assembled structure. As a first step towards addressing this shortcoming, we experimentally and computationally investigate the single interaction of the 1-decyl-3-methylimidazolium IL cation, $C_{10}mim^+$, paired with three different anions (Cl^-, NO_3^-, SCN^-) of varying size, symmetry and hydrogen bonding capacity in context with the self-assembled nanostructure.

Numerous theoretical studies, and simulations sometimes coupled with experiments, have been performed evaluating the liquid structure of neat ILs and have yielded important insights into IL properties and behaviour.[21] Molecular dynamics (MD) simulations assessing structural organization of imidazolium ILs in vacuum, cellulose, gases (*e.g.*, CO_2) and organic solvents (*e.g.*, acetonitrile) have been reported.[21] Comparatively, fewer studies have simulated the structure of imidazolium ILs in water. All-atom MD simulations carried out on water immiscible ILs (*i.e.*, 1-butyl-3-methylimidazolium hexafluorophosphate) showed, for example, that increasing water content did not act to significantly alter the distance between the anion and cation.[22] A finding that supported earlier MD simulations on 1-butyl-2,3-dimethylimidazolium bistrifluoromethanesulfonylimide aqueous mixtures was that water tends to self-cluster in these systems, acting to decrease organization between the cation and anion but not sufficiently so as to completely break charge ordering.[23] Classical MD and density functional theory on L-histidine derived imidazolium cations paired with either a bromide or bis(trifluoromethylsulfonyl)amide anion, revealed cation–anion coordination is more highly perturbed by water for compositions possessing the hydrophilic bromide and less so for the hydrophobic NTF_2 anions.[24] MD simulations on 1-butyl-3-methylimidazolium iodide disclosed that physical properties such as melting point, viscosity and ionic conductivity were all highly water content dependent.[25] Specifically, the simulations showed ordering mediated by iodide–water hydrogen bonding up to 50 mol % water, causing an increase in melting point, viscosity and reduction ion conductivity. In compositions above 50 mol% water the iodide becomes fully water solvated and the mixture resembles bulk water with dissolved IL, leading to a decrease in melting point, viscosity and increased conductivity.[25] Dhungana *et al.* carried out MD simulations in concert with X-ray scattering studies on 1-ethyl-3-methylimidazolium paired with a collection of cyano-anions and established a correlation between anion size, ion ordering, and sample viscosity.[26] The general finding was that the larger the anion, the more likely it orients radially with respect to the cation.[26] While these aforementioned studies primarily centred on solvent shell structure, MD simulations by Voth and co-workers examined 1-octyl-3-methylimidazolium nitrate using atomistic models coupled with MD simulations to gain insights into the molecular-level understanding of the underlying mechanism of nanostructural organization.[27] Greatest nanoscale ordering was achieved when the hydrogen bonding ability of the anion was saturated by water.[27] All of these aforementioned studies on water miscible ILs point toward highly complex interactions, justifying continued studies that strive to more fully bridge molecular-level (short-range) structure with nanoscale organization.

To address this void we examine the application of the Effective Fragment Potential (EFP) method, using polarizable terms to study the 1,3-dialkylimidazolium cation paired with hydrophilic anions in high molar ratio water mixtures. MD simulations (up to nanoseconds) were carried out using the EFP method, a computationally inexpensive way of modeling intermolecular interactions in non-covalently bound systems. Application of the EFP method for simulating interactions between molecules has been an active area of research applied to both Quantum Mechanical/Molecular Mechanical (QM/MM) systems and stand-alone molecular dynamics and Monte Carlo simulations.[28,29] EFP breaks down the interaction energy between two fragments into electrostatic, polarization, dispersion, and exchange repulsion terms. Each fragment is represented through distributed electrostatic multipole analysis, polarizabilities localized at molecular orbital centroids, and Gaussian exchange repulsion functions. Single QM calculations, without user adjustments, generate the parameters that comprise a single fragment. This allows the method to be flexible for simulating new or unexplored systems for which generating a classical MM force field would be time consuming. Furthermore, since the QM calculations used to parameterize EFP do not require user input, they are of consistent quality when generated for new systems. This fact, along with the inclusion of polarizabilities in the model makes EFP an ideal candidate for exploring and rapidly characterizing new IL systems.

The EFP methodology has previously been applied to the study of ILs, specifically, the 1,3-dimethylimidazolium cation, paired with halides, simulated in an anhydrous box.[30] These studies showed good agreement between Radial Distribution Functions (RDFs) generated by EFP and those produced by both higher-level theoretical models and neutron diffraction experiments. Although Tan and Izgorodina reported that EFP applied to ionic systems does yield errors in comparison to high level *ab initio* calculations, the errors are less than those found using force-field parameters optimized for ionic liquids as demonstrated in Table S1.†[31] Recent developments in the EFP methodology have made it possible to study flexible fragments.[32] This approach is predominantly meant for the study of macromolecules such as proteins and peptides, and the usefulness of this method for accurately studying ILs containing long alkyl chains is obvious and validated here. Herein, simulations are validated against experiments, including ^{1}H NMR and synchrotron X-ray scattering. This comprehensive approach is designed to eliminate the shortcomings of prior studies.

Experimental

Materials

1-Decyl-3-methylimidazolium bromide was purchased from EMD chemicals (Savannah, GA). 1-Decyl-3-methylimidazolium chloride was purchased from Ionic Liquid Technologies Inc. (Tuscaloosa, AL). Sodium thiocyanate (NaSCN) was purchased from Alfa-Aesar (Lancashire, UK). Dichloromethane (CH_2Cl_2), diethyl ether (Et_2O) and acetone ($(CH_3)_2CO$) were purchased from VWR (Radnor, PA).

Silver nitrate ($AgNO_3$) was purchased from Sigma Aldrich (Milwaukee, WI, USA). All reagents were of reagent grade or better and used as received. Milli-Q (18 MΩ) water (H_2O) was used where applicable.

Ionic liquid synthesis

1-Decyl-3-methylimidazolium thiocyanate, $C_{10}mim^+SCN^-$. Sodium thiocyanate (0.600 g, 6.93 mmol) was added to a solution of 1-decyl-3-methylimidazolium bromide, $C_{10}mim^+Br^-$ (2.00 g, 6.60 mmol), in acetone (60 mL) and stirred overnight at rt under an Ar atmosphere. The reaction mixture was filtered to remove NaBr and acetone was removed under reduced pressure. CH_2Cl_2 (50 mL) was added to precipitate excess NaSCN, and the mixture was filtered and residual CH_2Cl_2 removed under reduced pressure. The product was dried under vacuum for 24 h at 60 °C giving 1.70 g of a viscous light red liquid (yield 92%). Mp: −6.7 °C (DSC). ^1H NMR (500 MHz, $CDCl_3$) δ (ppm): 9.48 (s, 1H), 7.35 (s, 1H), 7.30 (s, 1H), 4.31 (t, $J = 7.5$ Hz, 2H), 4.12 (s, 3H), 1.93 (tm, 2H), 1.35 (tm, 2H), 1.25 (m, 12H), 0.87 (t, $J = 6.5$ Hz, 3H). ^{13}C NMR (500 MHz, $CDCl_3$) δ (ppm): 137.2, 131.9, 123.5, 121.9, 50.5, 36.8, 30.2, 29.4, 29.3, 29.2, 28.9, 26.3, 22.6, 14.1. ATR/FT-IR (cm^{-1}): 3085, 2922, 2955, 2852, 2050, 1572, 1462, 1165, 744, 620. Anal. calcd for $C_{15}H_{27}N_3S\cdot0.25H_2O$: C, 63.00; H, 9.69; N, 14.69; S, 11.21; found: C, 62.89; H, 9.94; N, 14.80; S, 11.53. Ion chromatography for bromide ion: 0.679%.

1-Decyl-3-methylimidazolium nitrate, $C_{10}mim^+NO_3^-$. 1-Decyl-3-methylimidazolium bromide, $C_{10}mim^+Br^-$ (2.00 g, 6.60 mmol), was added into a pre-weighed 100 mL round-bottom flask and dried overnight under vacuum at 100 °C. The mass of the dried 1-decyl-3-methylimidazolium bromide was re-determined as 1.95 g. Then, silver nitrate (1.10 g, 6.44 mmol) was added to a solution of the $C_{10}mim^+Br^-$ (1.95 g, 6.44 mmol) in nanopure H_2O (60 mL) and stirred overnight at rt under an Ar atmosphere. The reaction mixture was protected from light by wrapping the flask in aluminium foil. The mixture was filtered through Celite to remove bulk AgBr. The recovered hazy suspension was centrifuged (5000 rpm for 10 min) to remove additional AgBr. The supernatant was decanted into a new centrifuge tube and the process was repeated until no additional precipitate was visually observed. As a further test for removal of AgBr, the aqueous solution was stored in the dark for 3 days at room temperature and centrifuged one last time. It is important to note that this does not imply the complete absence of bromide ion, as the minimum achievable level of bromide contamination is dictated by the solubility product constant of AgBr in water, 5.2×10^{-13}.[33] Water was removed at 100 °C in an open beaker in the dark. The product was then re-dissolved in CH_2Cl_2 (50 mL) to precipitate any remaining $AgNO_3$. The mixture was filtered again and CH_2Cl_2 was removed under reduced pressure. The product was dried *in vacuo* for 24 h at 60 °C yielding 1.49 g of a viscous pale yellow liquid (yield 82%). This procedure did not lead to darkening of the product upon exposure to sunlight, an indication that Ag salts were effectively removed. Mp: 17.8 °C (DSC). ^1H NMR (500 MHz, $CDCl_3$) δ (ppm): 9.95 (s, 1H), 7.39 (s, 1H), 7.30 (s, 1H), 4.21 (t, $J = 7.3$ Hz, 2H), 4.01 (s, 3H), 1.87 (m, 2H), 1.31 (m, 2H), 1.28 (m, 12H), 0.86 (t, $J = 6.8$ Hz, 3H). ^{13}C NMR (500 MHz, $CDCl_3$) δ (ppm): 138.3, 123.4, 121.8, 50.2, 36.3, 30.2, 29.4, 29.3, 29.2, 28.9, 26.2, 22.6, 14.1. ATR/FT-IR (cm^{-1}): 3094, 2955, 2922, 2853, 1567, 1450, 1331, 1167, 829, 623. Anal.

calcd for $C_{15}H_{27}N_3S \cdot 0.75H_2O$: C, 56.26; H, 9.61; N, 14.06; found: C, 56.42; H, 9.79; N, 14.24. Ion chromatography for bromide ion: <47 ppm.

Physical methods

Elemental analysis was performed by Galbraith Laboratories, Inc. (Knoxville, TN). Attenuated total reflectance/Fourier transform-Infrared (ATR/FT-IR) spectroscopy was performed using a Thermo-scientific Nicolet 6700 spectrometer equipped with a diamond ATR crystal. Data were collected from 4000 to 500 cm^{-1} with a resolution of 2 cm^{-1} and averaged over 512 scans. The amount of residual water in the synthesized ionic liquids was determined by thermogravimetric analysis (TGA), carried out on a TA instruments Q500 instrument, by heating a known amount of sample (2–5 mg) from 25 °C to a final temperature of 600 °C at a rate of 5 °C min^{-1} under N_2 flow. TGA studies were carried out for synthesized IL samples after being dried overnight under vacuum at 100 °C. The water content was calculated using the initial weight loss up to 150 °C. The residual water contents were reported for 1-decyl-3-methylimidazolium nitrate, $C_{10}mim^+NO_3^-$; 1-decyl-3-methylimidazolium thiocyanate, $C_{10}mim^+SCN^-$; and 1-decyl-3-methylimidazolium chloride, $C_{10}mim^+Cl^-$ as 0.92% (w/w), 4.9% (w/w) and 2.0% (w/w), respectively. Differential scanning calorimetry (DSC) was performed on all dried (yet retaining residual water) synthesized ionic liquids using a TA instruments Q100 that was interfaced with a refrigerated cooling system. Instrument calibration was performed using an indium standard. Weighed amounts (5–10 mg) of the polymer and composite were sealed in aluminum pans and equilibrated at −75 °C for 5 min prior to starting the heating/cooling cycle collected at 2 °C min^{-1}. Polarized optical images were collected on a Meiji (San Jose, CA) ML-9300 polarized optical microscope at room temperature using an HD-1000 LITE digital camera. The camera was operated using ISCapture Software that was provided by the manufacturer. Samples were prepared by placing a small quantity of the IL–water mixture on a clean microscope slide. A coverslip was placed over the sample and light pressure was applied to create a level sample that was then visualized under polarized light.

^1H NMR spectroscopy was performed on a Bruker Avance 500 instrument at a magnetic field strength of 11.7 T (^1H frequency of 500.13 MHz) using a tuneable 5 mm broadband probe with ^2H lock at 76.773 MHz. The nature of the water–IL interactions leading to gelation was probed by examining the effect of water addition upon the chemical shift of the protons of $C_{10}mim^+$ for $C_{10}mim^+A^-$ ($A = Cl^-$, SCN^- and NO_3^-). In an initial series of experiments, increasing quantities of water were added to weighed samples of $C_{10}mim^+A^-$ dissolved in CD_3CN in a NMR tube, and the mixtures were repeatedly warmed and mixed in an effort to obtain uniform samples. The solutions were then titrated with additional water added using a metered glass syringe, and the chemical shifts of the C-2 proton of $C_{10}mim^+$ were measured as a function of water concentration. The small amount of non-deuterated acetonitrile present in CD_3CN and the small amount of non-deuterated chloroform present in $CDCl_3$ were used as the internal references for the chemical shift determination. (All spectra were referenced to $CDCl_3$ (7.26 ppm) and CD_3CN (1.94 ppm).) Because the IL contains a trace amount of water even after prolonged oven drying, the total water content of samples containing low added-water-to-IL ratios was determined by integration of the NMR spectrum.

Small-angle X-ray scattering (SAXS) measurements were performed using the pin-hole set-up at the undulator beamline 12ID at the Advanced Photon Source (APS) at Argonne National Laboratory (Lemont, IL). Data collected at station C (12 keV) used a custom built CCD detector composed of 4 CCD chips and features a 180 mm square active area with 1024 × 1024 pixel resolution. The sample-to-detector distance provided a q-range from 0.025–0.6 Å^{-1}. Wide-angle X-ray (WAXS) data was collected either at station B (14 keV) using a Pilatus 300K (Dectris, Baden-Daettwil, Switzerland) or at station C (18 keV) using the custom built CCD detector as described above. For all SAXS measurements the scattering vector, q, was calibrated with silver behenate employing the characteristic diffraction ring at $q = 0.1076\ \text{Å}^{-1}$. For WAXS studies the scattering vector, q, was calibrated with cerium oxide. The collected scattering images were averaged to produce plots of scattering X-ray intensity, $I(q)$, *versus* the scattering vector, q, where $q = 4\pi \sin(\theta)/\lambda$. IL/$H_2O$ binary mixtures were prepared by combining weighed quantities of water and the desired IL. To ensure the mixtures were homogenous, repeated vigorous mixing was required. Gentle warming, by reducing the viscosity of the mixture, facilitated the homogenization. The samples were sealed in Pasteur pipettes for all X-ray measurements. All measurements were made at 22 °C (±1 °C).

Theoretical methodology

Effective fragment potential. Effective Fragment Potential (EFP) parameters were generated for all IL anions (Cl^-, NO_3^-, SCN^-), and water using the Gamess computational chemistry suit.[34] Briefly, molecular structures were obtained from Density Functional Theory (DFT) calculations performed with a ωB97-x functional in the 6-31+G* basis set.[35] From the optimized structures, EFP parameters were generated using standard EFP calculations available in Gamess.[34] Due to extremely large values, a scaling factor of 0.6 was applied to the SCN^- polarizabilities to prevent polarization catastrophes during the MD simulations. 3-Methyl-1-pentylimidazolium, a cation with a shorter alkyl chain than experimentally used in this study, was selected as a means to reduce the size of the box necessary for the calculations. Yet, even with the shorter alkyl chain, employing a single ridged EFP fragment did not accurately represent the behaviour of the cation in water. Thus, the recently developed procedures for applying EFP to macromolecules were implemented.[32] This procedure introduces some degree of flexibility to the cation by splitting the molecule into two separate EFP potentials at the nitrogen–carbon bond between the imidazolium head group and pentyl tail. The sub-fragments were capped with hydrogen atoms and EFP parameters were generated using Gamess. Charge and polarization terms for the capping hydrogen were removed from the fragment parameter sets and the excess charge (0.43 e^- for the head group and 0.22 e^- for the alkyl chain) was equally redistributed to each atom in the truncated fragment. The charge on the tail is set explicitly to 0 and the charge on the head group to +1. A classical bond between the carbon and nitrogen atoms using the following parameters joined the two fragments: bond length, force constant, and angles. These parameters were obtained from the Tinker general atom force field.[36] The EFP method is designed to accurately model intermolecular interactions and thus is not suited for computing interactions between fragmented molecules.[28] For this reason, interactions between these two fragments were explicitly ignored in the EFP code, thus the two fragments interact strictly through the classical force-field.

Molecular dynamics. For each anion, five different random orientations of anion and 3-methyl-1-pentylimidazolium were placed in a box of size 21.5 Å. The boxes were then solvated with an equivalently sized box of water equilibrated for 1 ns. 20 independent trajectories were run, five for each anion. Each trajectory went through 5 cycles of 0.2 ns annealing at 375 K, 0.2 ns of equilibration at 310 K, and then 0.2 ns of data collection, resulting in a total of 1 ns of usable data from each trajectory. A total of 5 ns of data were collected for each ionic species, which is comparable with other MD simulations performed with force-field methods. All MD simulations used an NVT ensemble. An equilibration time of 0.2 ns was demonstrated to be sufficient to return the water self-diffusion coefficient to a steady value, as shown in Fig. S1.† MD simulations on bulk water determined the water self-diffusion coefficient at various temperatures, which are shown in Table S2.† The purpose of these simulations was to determine the temperature at which to run the simulations to give a reasonable replication of the bulk water self-diffusion constant. To more accurately reproduce the experimentally determined room temperature bulk diffusion coefficient for water ($0.23\ \text{Å}^2\ \text{ps}^{-1}$),[37] all further simulations were run at 310 K. All MD simulations were performed with libEFP[38] interfaced with Tinker 6.0 (ref. 36) to compute contributions from the single force field bond.

NMR simulations. The MD trajectories were scanned for frames where the anion was either in close proximity to (first solvent shell) or some distance from (greater than 7 Å away from) the C-2 proton. The close proximity frames were labelled as "low water" and the distant frames were labelled as "high water". The cation, anion, and ten nearest water molecules to the C-2 proton were extracted from the MD trajectory and fed into the Gaussian quantum chemistry package.[35] These simulations were carried out by using the ωB97-x functional in the 6-31+G* basis set.[39] A reference of 31.756 for tetramethylsilane was used to convert the calculated values into chemical shifts in ppm.

Results and discussion

As a critical first step towards advancing our understanding of the relationship between amphiphilic ionic liquid (IL) molecular structure and nanoscale self-assembled architectures produced upon dispersal in water, we examine here the 1-decyl-3-methylimidazolium, $C_{10}mim^+$, (1), cation experimentally and compare these results with theoretical studies on the less computationally intensive 3-methyl-1-pentylimidazolium, C_5mim^+, paired with three different anions. Three hydrophilic monovalent anions of varying geometries and basicities were selected; spherical chloride (Cl^-), trigonal planar nitrate (NO_3^-), and linear thiocyanate (SCN^-).[40,41] The alkyl chain mismatch (C-5 *vs.* C-10) between theory and experiments is inconsequential in the present study since simulations were on a single ion pair solvated in water. The primary focus of this report is evaluation of the cation head group–anion pairing, solvation, and hydrogen bonding, and relating those findings to the nanoscale structure induced by the addition of water. Future studies will evaluate the intermediate and long-range ordering between ensembles of ILs.

The ILs experimentally studied were either used as received from commercial sources (*i.e.*, $C_{10}mim^+Cl^-$) or prepared *via* metathesis reactions involving treatment of solutions of commercially received $C_{10}mim^+Br^-$ with $AgNO_3$ or NaSCN to yield $C_{10}mim^+NO_3^-$, and $C_{10}mim^+SCN^-$, respectively. Nuclear magnetic resonance (NMR) spectroscopy, vibrational (FT-IR) spectroscopy, and combustion analysis coupled with ion chromatography confirmed the success of the anion exchange. In the case of $C_{10}mim^+NO_3^-$, the appearance of a strong vibrational mode at 1332 cm^{-1} for N–O stretching was used as an indicator for the presence of nitrate (Fig. S2A†).[42] In the case of $C_{10}mim^+SCN^-$, the appearance of a strong vibration mode at 2050 cm^{-1} for C=N stretching (Fig. S3A†) was used as an indicator for the presence of SCN^- as well as ^{13}C NMR showing the resonance at 131.9 ppm (Fig. S3C†) being indicative of the presence of SCN^-.[43] Combustion analyses were within acceptable limits (±0.3%) when accounting for trace water in the molecular formula, and ion chromatography determined that less than 47 ppm of bromide anion remained for $C_{10}mim^+NO_3^-$ and 0.7% of bromide anion remained for $C_{10}mim^+SCN^-$, confirming successful anion exchange. In this study we limit our discussion to IL/water binary mixtures that represent a low and high dilution state.

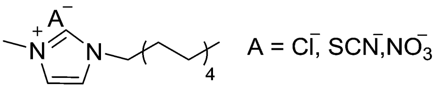

(1)

Macroscopic properties/nanoscopic structure

Aqueous mixtures of $C_{10}mim^+SCN^-$ studied over a range of water contents (4.9% (w/w), 0.45 mole fraction H_2O; 20.8% (w/w), 0.80 mole fraction H_2O; 23.7% (w/w), 0.83 mole fraction H_2O; 34.7% (w/w), 0.89 mole fraction H_2O; 58.9% (w/w), 0.96 mole fraction H_2O) were macroscopically homogenous, transparent and pale orange in colour. $C_{10}mim^+SCN^-$ dried under vacuum, but still retaining residual 4.9% (w/w) H_2O as determined by thermogravimetric analysis (Fig. S4A†), possessed a very low melting point, −6.7 °C, as determined by DSC (Fig. S4B†). As previously noted, IL melting points are mainly determined by the molecular architecture of the cation and anion and the interaction between them.[7,32] The low melting point observed here suggests weak coulombic forces between $C_{10}mim^+$ and SCN^-. Further indication of weakened anion–cation–solvent interactions is found in the sample viscosity. The three lowest water content compositions (4.9–23.7% (w/w)) were weak physical gels. At higher water content (34.7% (w/w); 58.9% (w/w)) samples were visually observed to be free flowing liquids and thus defined a high dilution state. The lack of strong physical gel formation (defined here as a sample having a glassy-like appearance and resistant to flow upon inversion) over the entire range of compositions is notably different than previous IL compositions prepared with $C_{10}mim^+$ and implies weak ionic domain interactions and the absence of an extended hydrogen-bonded network.[7] The observed collection of properties also implies diminished structural heterogeneity. The deficiency in nanoscale structure is supported, in part, by the absence of optical birefringence when a thin film of each composition is viewed under polarized light (data not shown). Small-angle X-ray scattering (SAXS) provided greater details on the lyotropic mesophase structure. The 2-D SAXS patterns on all compositions examined were found to be composed of isotropic diffraction rings, signifying poor spatial coherence (data not shown). The 1-D scattering curves for the $C_{10}mim^+SCN^-$: H_2O mixtures examined at three water contents (low dilution,

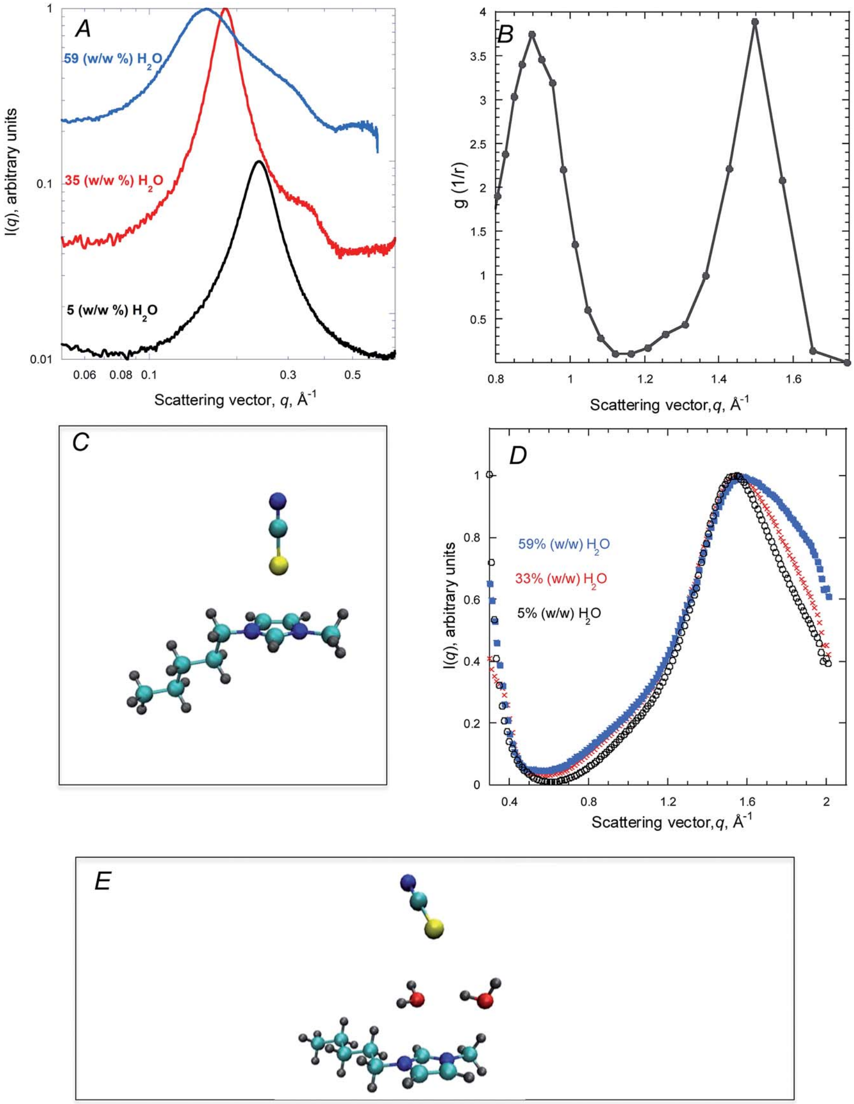

Fig. 1 (A) Small-angle X-ray scattering (SAXS) curve collected on $C_{10}mim^+SCN^-$ ILs at 4.9% (w/w) H_2O (black curve), 34.7% (w/w) H_2O (red curve) H_2O, and 58.8% (w/w) (blue curve). (B) Theoretically determined radial distribution function (RDF) for single cation C_5mim^+ to single anion SCN^-. (C) Commonly determined geometric configuration of the first solvent shell structure as determined by MD simulations. (D) Wide-angle X-ray scattering (WAXS) data collected on $C_{10}mim^+SCN^-$ ILs at 4.9% (w/w) H_2O (black curve), 34.7% (w/w) H_2O (red curve), and 58.8% (w/w) (blue curve). (E) Commonly determined geometric configuration of the second solvent shell structure as determined by MD simulations.

4.9% (w/w); high dilution, 34.7% (w/w) and 58.9% (w/w)) are shown in Fig. 1A (black, red, blue curves respectively). The breadth of the diffraction features again confirms the lack of well-ordered mesophases. For the low dilution state (4.9% (w/w)), the weakest ordering was verified by the presence of a single, broad diffraction peak at $q = 0.238$ Å^{-1} ($d = 26.4$ Å) (Fig. 1A, black curve). Increasing the water to 20.8–23.7% (w/w) improved structural ordering, indicated by the appearance of an additional diffraction feature in the high q region (data not shown). At 34.7% (w/w) water the primary diffraction peak shifts to $q = 0.181$ Å^{-1} ($d = 34.7$ Å) and a discernible shoulder is found at $q \sim 0.36$ Å^{-1}, confirming the mesophase structure is a weakly ordered lamellar structure (Fig. 1A, red curve). At the highest water content, 58.9% (w/w), the primary peak shifts further towards the low q region of the SAXS pattern ($q = 0.157$ Å^{-1}; $d = 40.0$ Å) and both the peak and shoulder become broader. As expected, increasing the water content in the binary mixtures from 4.9% (w/w) to 58.9% (w/w) serves to increase the lattice spacing (from 26.4 Å to 40.0 Å). Remarkably, a macroscopic change in the sample viscosity does not correlate with the determined nanoscale structure. That is, a sample of low viscosity (liquid-like), at 34.7% (w/w) water, shows a greater degree of ordering (*i.e.*, fidelity and symmetry) than the low dilution sample (4.9% (w/w)), which was a weak physical gel. This observation implies a complex ionic domain environment that is highly water dependent.

Lastly, unlike many ILs containing short alkyl chains, it is noted that irrespective of the composition, the SAXS patterns do not show a “pre-peak” located between $q \sim 0.4$–0.6 Å^{-1} for $C_{10}mim^+SCN^-$: H_2O mixtures.[16,44] The origin of the familiar “pre-peak” remains highly debated in the literature but has been assigned to the intramolecular distance between the cation ring and the terminal methyl group on the alkyl chain as well as other short range ordering.[45] The absence of this structural correlation is noted here and may be due to the greater long-range structural ordering achieved in these binary mixtures. To better evaluate the origin of the pre-peak in aqueous ionic liquid mixtures, MD simulations employing the EFP potential on ensembles are currently underway.

Aqueous mixtures of $C_{10}mim^+NO_3^-$ were similarly studied at select water contents ranging from 0.92% (w/w) (0.13 mole fraction H_2O) to 47.6% (w/w) (0.94 mole fraction H_2O). All compositions within this range of water were macroscopically homogeneous, transparent and pale yellow in colour. Samples ranging from 19.2% (w/w) to 35.1% (w/w) H_2O were found to visually form strong physical gels. At 41.4% (w/w) H_2O the sample was a weak physical gel, while the 47.6% (w/w) water sample was a free flowing liquid. $C_{10}mim^+NO_3^-$ dried under vacuum, retaining a residual 0.92% (w/w) H_2O (Fig. S5A†), and had a melting point of 17.8 °C (Fig. S5B†), a value markedly higher than that determined for $C_{10}mim^+SCN^-$. The increased melting point and viscosity signal the existence of increased anion–cation–solvent interactions. The polarized optical micrograph collected on a thin film of the composition composed of 19.2% (w/w) (0.79 mole fraction H_2O) shows strong optical birefringence confirming the presence of a liquid crystalline phase (Fig. 2A).[46] Representative 1-D SAXS patterns collected on $C_{10}mim^+NO_3^-$ at 19.2% (w/w) and 41.4% (w/w) H_2O are presented in Fig. 3A (red and blue curves, respectively). The 1-D pattern at 19.2% (w/w) H_2O displays two sharp diffraction peaks at $q = 0.212$ ($\sqrt{1}$) Å^{-1}; 0.370 Å^{-1} ($\sqrt{3}$), indexing to a 2D hexagonal lattice with a d-spacing of 30.0 Å. Examination of the corresponding 2-D SAXS pattern allows for more accurate assignment of the symmetry/structural

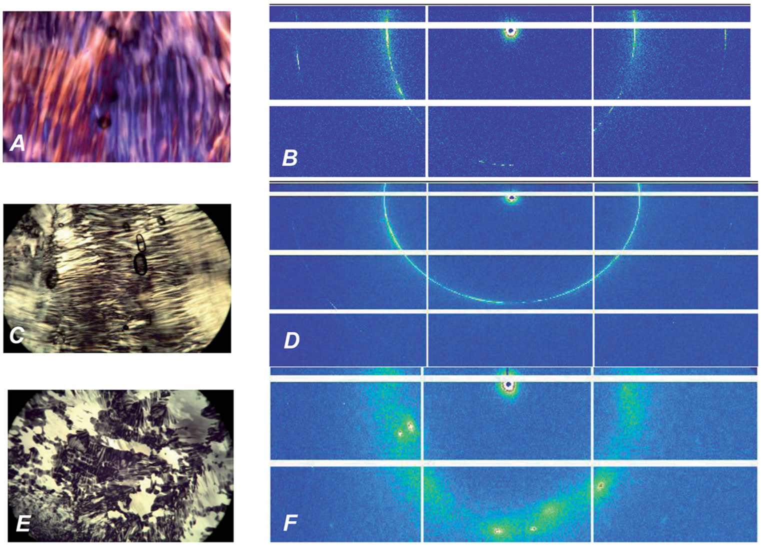

Fig. 2 (A) Polarized optical microscopy (POM) image and (B) 2-D SAXS pattern for $C_{10}mim^+NO_3^-$ at 19.2% (w/w) H_2O. (C) POM micrograph and (D) 2-D SAXS pattern collected on $C_{10}mim^+Cl^-$ ILs at 14.1% (w/w) H_2O. (E) POM micrograph and (F) 2D SAXS pattern collected on $C_{10}mim^+Cl^-$ at 43.8% (w/w) H_2O. Magnification was 107×.

motif (Fig. 2B). Here, the 2-D pattern is strongly anisotropic with the scattered X-ray intensity directed predominantly along the equatorial axis, a signature for the existence of a modulated lamellar structure (HML). Modulated and perforated lamellar structures have been previously observed to form in vinyl IL monomers, $C_{10}Vim^+A^-$ aqueous mixtures.[47] The HML structure is a structure intermediate in character between a lamellar and columnar phase. This morphology is composed of lamellar sheets that contain in-plane modulations (or partial perforations) centred on a hexagonal lattice. At high dilution, (41.4% (w/w) H_2O), as anticipated, a loss of structural ordering is found. The 2-D SAXS pattern is isotropic (data not shown) and the 1-D scattering curve (Fig. 3A, blue curve) displays two broad features at $q = 0.184$ Å^{-1} ($\sqrt{1}$) and 0.323 Å^{-1} ($\sqrt{3}$), signalling a 2D hexagonal micellar structure. Loss in the fidelity of nanoscale ordering at high water content for $C_{10}mim^+NO_3^-$ is consistent with the observed lower viscosity (liquid) and suggests excess water acts to weaken ion pair association and disrupt hydrogen bonding.

Aqueous mixtures of $C_{10}mim^+Cl^-$ studied over the range of 14.1% (w/w) (0.70 mole fraction H_2O) to 43.8% (w/w) (0.92 mole fraction H_2O) were all also visually found to be macroscopically uniform, colourless strong physical gels. The melting point for the dried $C_{10}mim^+Cl^-$, but retaining a residual 2.0% (w/w) H_2O (0.23 mole fraction H_2O) (TGA shown in Fig. S6A†) was significantly higher than that determined for the other ILs at 27.5 °C (Fig. S6B†). These properties confirm strong interactions within the ionic domain of $C_{10}mim^+Cl^-$. When viewed under polarized light, the samples composed of 14.1% (w/w) and 43.8% (w/w) H_2O display strong optical birefringence (Fig. 2C and E, respectively), denoting well-ordered nanostructures. Specifically, at 14.1% (w/w) the texture is mosaic,

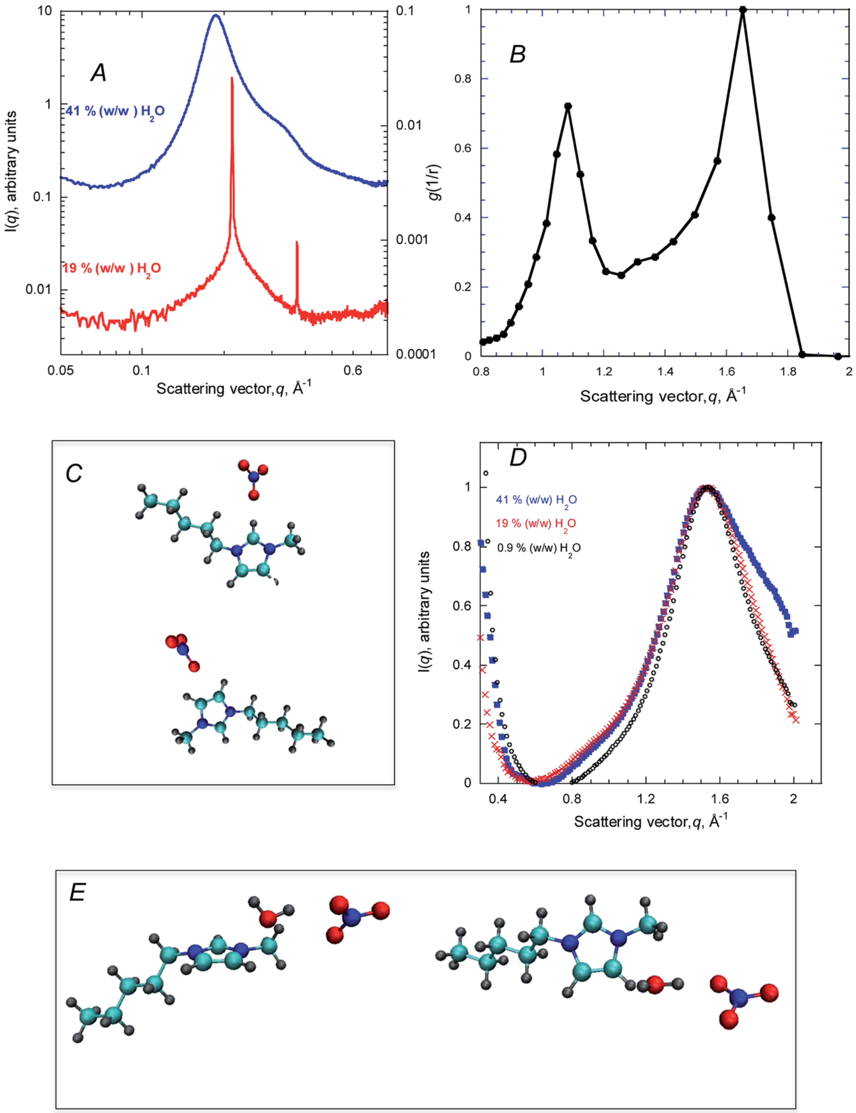

Fig. 3 (A) Small-angle X-ray scattering (SAXS) curve collected on $C_{10}mim^+NO_3^-$ ILs at 19.2% (w/w) H_2O (red curve) and 41.4% (w/w) H_2O (blue curve). (B) Theoretically determined radial distribution function (RDF) for single cation C_5mim^+ to single anion NO_3^-. (C) Common geometric configuration of the first solvent shell structure as determined by MD simulations. (D) Wide-angle X-ray scattering (WAXS) data collected on $C_{10}mim^+NO_3^-$ ILs at 0.92% (w/w) H_2O (black curve), 18.9% (w/w) H_2O (red curve) and 41% (w/w) H_2O (blue curve). (E) Common geometric configuration of the second solvent shell structure as determined by MD simulations.

similar to those observed for the low dilution nitrate IL (19.2% (w/w) H_2O), suggesting the existence of a 2D hexagonal liquid crystalline phase. The 1-D SAXS profile collected at 14.1% (w/w) H_2O shows two sharp Bragg reflections at $q = 0.220$ ($\sqrt{1}$), 0.382 ($\sqrt{3}$) Å^{-1}, confirming a 2D hexagonal structure (Fig. 4A, red

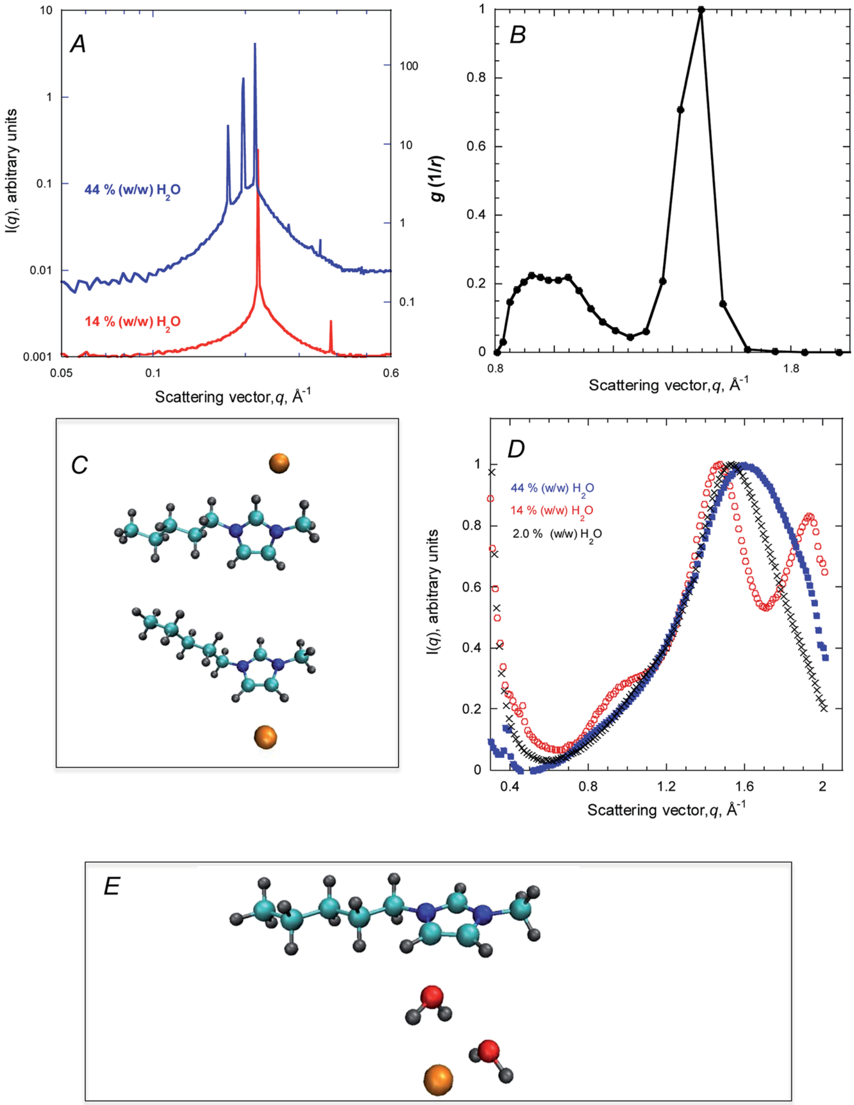

Fig. 4 (A) Small-angle X-ray scattering (SAXS) curve collected on $C_{10}mim^+Cl^-$ ILs at 14.1% (w/w) H_2O (red curve) and 43.8% (w/w) H_2O (blue curve). (B) Theoretically determined radial distribution function (RDF) for single cation C_5mim^+ to single anion Cl^-. (C) Common geometric configuration of the first solvent shell structure as determined by MD simulations. (D) Wide-angle X-ray scattering (WAXS) data collected on $C_{10}mim^+Cl^-$ ILs at 2.0% (w/w) H_2O (black curve), 14.1% (w/w) H_2O (red curve) and 43.8% (w/w) H_2O (blue curve). (E) Common geometric configuration of the second solvent shell structure as determined by MD simulations.

curve). The *d*-spacing is 28.6 Å giving a lattice constant, *a*, of 33.0 Å. The observed 2D hexagonal structure is consistent with prior studies evaluating mesophase structure in binary mixtures of $C_{10}mim^+Cl^- : H_2O$.[12] It is further noted that a pure 2D hexagonal structure is formed by evaluation of the 2-D SAXS pattern, which does not display an equatorially aligned pattern. In prior work, we more fully evaluated a range of water contents between 39–42% (w/w) and reported the coexistence of cubic mesophase structures.[12] In this study, we similarly find at 43.8% (w/w) H_2O evidence of mesophase conversion to high symmetry, cubic structures. The 1D SAXS curve shows multiple sharp Bragg reflections located at $q = 0.173, 0.196, 0.214, 0.278, 0.332, 0.352$ Å^{-1} (Fig. 4A blue curve). The reflections can be indexed to coexisting discrete cubic phase ($q = 0.19$ ($\sqrt{2}$), 0.27 ($\sqrt{4}$), 0.35 ($\sqrt{8}$) Å^{-1}) and to the double diamond ($Pn3m$) structure $q = 0.17$ ($\sqrt{2}$), 0.21 ($\sqrt{3}$), 0.28 ($\sqrt{6}$), 0.33 ($\sqrt{8}$) Å^{-1}.[48] The polarized optical image collected on this sample is also suggestive of the coexistence of two mesophases (Fig. 2E). Here, the polarized optical image shows areas of low/absent birefringence (*i.e.*, darker regions consistent with a discrete cubic phase) interspersed with locations of high birefringence attributed to the double diamond phase. It should be noted that for lyotropic phases at higher water contents double diamond ($Pn3m$) phase formation is generally favoured.[49] On the other hand, the double diamond phase in thermotropic liquid crystals is less commonly observed.[50] As previously reported, very high water contents ~65% (w/w) are required for loss of gelation (conversion to a liquid) and transition to the 2D hexagonal micellar structure.[12]

Thus, the pairing of $C_{10}mim^+$ with SCN^-, a hydrophilic soft ion, does not produce strong physical gels at any water content. All $C_{10}mim^+SCN^- : H_2O$ binary mixtures are poorly ordered on the nano-length scale. Replacing SCN^-, with NO_3^- yields lyotropic mesophases exhibiting a range of viscosities and nanostructures. The use of Cl^-, a spherical compact anion, generates strong physical gels over a large region of the phase space examined, and self-assembles into well-ordered nanostructures of highly tuneable symmetries that are readily controlled by the amount of water in the binary mixtures.

Molecular level interactions

Experimental evaluation of ring proton shifts can be used to determine the relative strength of interactions between the respective anions and the imidazolium cation as a function of water content. ^1H NMR studies evaluating the chemical shift of the C-2 imidazolium ring proton for aqueous mixtures of $C_{10}mim^+A^-$, where $A^- = Cl^-, NO_3^-, SCN^-$, are presented in Fig. 5. Addition of water to acetonitrile solutions of the ILs causes a prominent up-field shift of the resonance for $C_{10}mim^+Cl^-$ (δ 10.1 ppm to 8.66 ppm for 1.4% (w/w) to 75.0% (w/w) H_2O, $\Delta\delta = 1.44$ ppm). Although to a lesser extent, the C-2 proton resonance for $C_{10}mim^+NO_3^-$ also shifts up-field with increasing water (δ 9.25 ppm to 8.63 ppm for 0.92% (w/w) to 77.0% (w/w), $\Delta\delta = 0.62$ ppm). The C-2 proton, which is significantly de-shielded at low dilution, becomes more shielded at high dilution.[7] The fact that the initial chemical shift for low dilution $C_{10}mim^+Cl^-$ is greater in magnitude than that determined for $C_{10}mim^+NO_3^-$ indicates that the interaction with the C-2 proton is greater for chloride than nitrate, an expected observation given the greater basicity of Cl^- *vs.* NO_3^-.[40,41] Furthermore, this observation correlates well with a previous study that established a hydrogen bonding accepting (HBA) scale for anions[51] This scale determined that chloride has a stronger ability to hydrogen bond than nitrate. Up-field shifting of the C-4 and C-5 protons are also observed with the addition of water for $C_{10}mim^+Cl^-$ *vs.* $C_{10}mim^+NO_3^-$ but the magnitude of the shift is less, suggesting a lessening in the

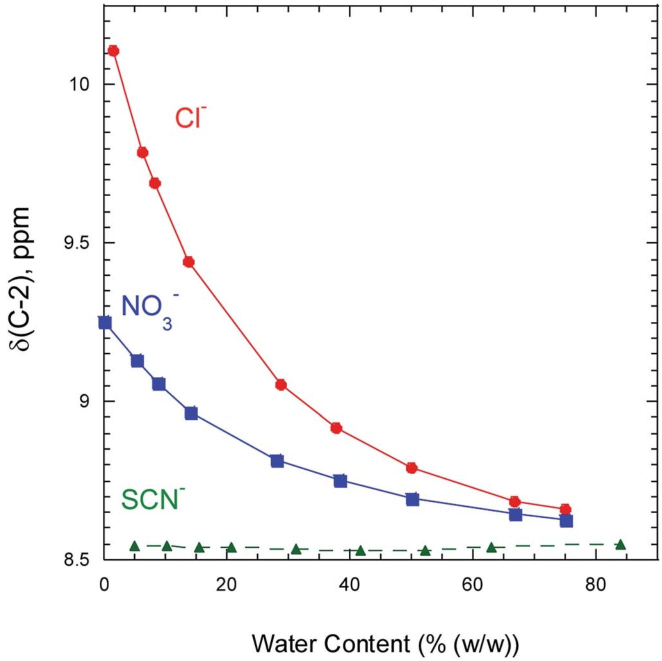

Fig. 5 ^{1}H NMR chemical shifts of the C-2 imidazolium proton for aqueous mixtures of $C_{10}mim^+A^-$, where $A^- = Cl^-$, NO_3^-, SCN^-.

interaction. Conversely, no shifting in the C-2 proton resonance with increasing water content is observed for $C_{10}mim^+SCN^-$. That is, the C-2 proton resonance remains nearly invariant at δ 8.5 ppm over the entire range of water contents studied (Fig. 5). This observation is consistent with work demonstrating that thiocyanate is a substantially weaker hydrogen bonding acceptor than nitrate and further implies a lack of association with the imidazolium ring protons.[51]

Theoretically determined NMR shifts between a "low" dilution (first solvent shell location within the MD simulations) and a "high" dilution state (defined as the anion being located >7 Å away from the cation) are given in Table 1. The "low" dilution values determined by theory compare favourably with experimental resonances for binary mixtures composed of 15–20% (w/w) H_2O. That is, for $C_{10}mim^+Cl^-$ a $\Delta\delta = 0.74$ compares well with experimental resonance differences

Table 1 Average chemical shift in ppm for the C-2 proton computed using Gaussian from individual molecular dynamics frames. These data agree strongly with experimental results, with chloride having the largest change in chemical shift when near the C-2 proton, thiocyanate having almost no dependence on position, and nitrate being between the two

Water content	Chloride C-2 proton chemical shift (ppm)	Nitrate C-2 proton chemical shift (ppm)	Thiocyanate C-2 proton chemical shift (ppm)
Low	9.30	9.09	8.83
High	8.57	8.65	8.84

between 70% (w/w) and 20% (w/w) H_2O. Similarly, for $C_{10}mim^+NO_3^-$ a $\Delta\delta = 0.44$ would result from the differences between a high dilution state of 75% (w/w) and low dilution state of 15% (w/w). Theoretically predicted C-2 proton resonances for $C_{10}mim^+SCN^-$ compare very well with those determined experimentally, showing invariance with water content. Thus, theory correctly predicts that chloride produces a larger chemical shift with increasing water than nitrate, and the lack of a shift for thiocyanate. Collectively, experimental and theoretical NMR studies reveal that ion pair interaction strength varies depending on the nature of the anion and the amount of water in the binary mixtures.

The experimental NMR findings can be further explained in the context of molecular dynamics (MD) simulations, which provides the common (preferred) molecular configurations and insights on the solvent shell structure revealed through cation–anion radial distribution functions (RDFs). The theoretically calculated RDFs can then be directly compared to wide-angle X-ray scattering (WAXS) experiments that yield information on solvent shell structure. Through qualitative assessment of the MD trajectories, two possible preferred molecular configurations for ion pairing between the imidazolium head group and chloride anion (*i.e.*, the first solvent shell) were determined (Fig. 4C, top). The calculations confirm in plane Cl^- positioning and association with the imidazolium ring. The dominant interaction is between Cl^- and the C-2 proton of $C_{10}mim^+$, a result fully in agreement with NMR studies. The anion does interact, albeit to a lesser extent, with the C-4 and C-5 protons on the imidazolium ring (Fig. 4C, bottom). A single cation to an anion pair radial distribution function (RDF) was calculated employing the imidazolium ring as the geometric centre (Fig. 4B). The single $C_{10}mim^+$ to Cl^- RDF as a function of scattering vector, q, is presented in Fig. 4B and is directly compared against the WAXS patterns collected at 2.0% (w/w), 14.1% (w/w), and 43.8% (w/w) $H_2O : C_{10}mim^+Cl^-$ mixtures (Fig. 4D). The position of the ion pair peak in the RDF is at 4.22 Å ($q = 1.50$ Å^{-1}), a value that qualitatively agrees with other studies evaluating a wide range of other $C_{10}mim^+$ anion pairs and reporting it to be generally located at ~5 Å.[13] The peak value compares exceptionally well with the experimental WAXS data (Fig. 4D) that shows a correlation peak at $q = 1.53$ Å^{-1} ($d = 4.11$ Å) at 2.0% (w/w) $H_2O : C_{10}mim^+Cl^-$ mixture. At a water content of 14.1% (w/w) the WAXS pattern becomes more complex with the primary (anion to cation) peak located at $q = 1.47$ Å^{-1} ($d = 4.27$ Å) and a second (of nearly the same magnitude) peak located at $q = 1.93$ Å^{-1} ($d = 3.26$ Å). The significantly increased structure, as evidenced by the two well defined peaks in the WAXS pattern at 14.1% (w/w) H_2O, could be explained by the chloride ion occupying both the theoretically determined preferred imidazolium in-plane (*i.e.*, equatorial) position and some population of chloride residing axially, sitting directly over the imidazolium ring. We hypothesize that dual occupancy (*i.e.*, chloride residing in both equatorial and axial sites around the imidazolium ring) at 14.1% (w/w) H_2O content yields the highly ordered, 2D hexagonal mesophase determined by SAXS. Axial occupancy of the chloride ion might occur, and be required for the generation of multiple IL cation layers that assemble *via* an offset between the layers, thereby promoting the Cl^- of one layer to sit directly over the imidazolium of another layer. In this packing arrangement each imidazolium cation would retain the theoretically predicted favourable interaction with the C-2, C-4/C-5 ring protons, but multilayer organization would produce axial Cl^- interactions. IL assembly employing both equatorial and axial positioned chloride is supported by single point cation–anion simulations, which showed that optimal separation between the chloride ion and imidazolium head group would result in a correlation peak at *ca.* $q \sim 2.2$ Å^{-1} ($d \sim 3$ Å), a value consistent with the location of the high scattering vector feature in the WAXS pattern collected at 14.1% (w/w) $H_2O : C_{10}mim^+Cl^-$ (Fig. 4D, red curve).

Increasing the water content in the binary mixture to 43.8% (w/w) causes a shifting in the correlation peak position in the WAXS pattern to higher q at 1.60 Å^{-1} (3.93 Å). The observed shifting of the correlation peak to smaller dimensions with increasing water suggests an increase in density due to increased water within the first solvation shell.[23,52] The observed shifting to higher q (shorter dimensions) with increasing water fraction in binary mixtures has been theoretically found in DIM^+DMP^- pairs which tend to aggregate more closely as water concentration increases.[53]

MD simulations reveal a smaller fraction of chloride ions residing in a second solvent shell around the imidazolium cation interactions mediated by water molecules (Fig. 4E). Several water molecules located near the ions serve to make up a network, as depicted in Fig. 4E, illustrating an electrostatically optimized orientation. In the theoretically determined RDF (Fig. 4B) a second solvent shell structure is resolved at $q = 0.92$ to 1.09 Å^{-1}. The reduced peak magnitude, compared to the first solvent shell, signals a lower probability of Cl^- residing in the second solvent shell. While the second solvent shell structure is not clearly resolved in the corresponding WAXS pattern collected at either very low or high water content (2.0% (w/w) and 43.8% (w/w) H_2O), it is observed in the well-ordered 14.1% (w/w) H_2O composition (Fig. 4D). Here specifically, a broad, less intense peak (shoulder) is found between 0.7–0.11 Å^{-1}, centred at ~0.91 Å^{-1}, a location consistent with MD simulations.

Similar to Cl^-, the NO_3^- anion also preferentially associates with the imidazolium ring protons to comprise the first solvent shell, as determined by MD simulations (Fig. 3C). Here too, NO_3^- resides within the plane of the imidazolium ring with greater preference for association for the acidic C-2 proton compared to the C-4 and C-5 protons (Fig. 3C). The theoretically predicted distribution of the NO_3^- around the imidazolium determined using the EFP model differs from those reported by Voth and co-workers.[54] Voth and co-workers predicted no density of the NO_3^- anion at the C-4, C-5 protons of the imidazolium ring. Conversely the EFP model indicates a slight preference for NO_3^- at the C-2 proton over the C-4 and C-5 protons. The difference is attributed to a manifestation of the polarizability of the imidazolium ring in the EFP model, which facilitates stabilizing electrostatic interactions on the C-4 and C-5 side of the cation. A combined $C_{10}mim^+$ to oxygen of the NO_3^- anion RDF as a function of scattering vector, q, is presented in Fig. 3B and directly compared against the WAXS data collected at high (41.4% (w/w)) and low (19.2% (w/w); 0.92% (w/w)) dilution for $C_{10}mim^+NO_3^-$ (Fig. 3D). Oxygen atoms were chosen as the entity from which to compute the RDF since they possess the majority of the electron density, and therefore represent the scattering centres. The location of the primary solvent shell peak in the simulated RDF ($q = 1.65$ Å^{-1}; $d = 3.81$ Å) is due to a single nitrogen being hydrogen bound to the C-2 imidazolium ring proton. The second peak in the simulated RDF (at $q = 1.08$ Å^{-1}; $d = 5.82$ Å) is attributed to the two trailing oxygen atoms interacting with the surrounding water. The position of the first solvent shell ion pair peak in the theoretical RDF at low water content is a cation to anion separation larger than determined for the corresponding low dilution $H_2O : C_{10}mim^+Cl^-$ mixture. The increased ion pair separation indicates NO_3^- is less coordinating, forming a weaker association with $C_{10}mim^+$. The theoretical peak value compares well with the experimental WAXS data (Fig. 3D) which shows a correlation peak at $q = 1.52$ Å^{-1} ($d = 4.13$ Å). While the width and peak location of the theoretical RDF correlate well with the experimental WAXS data, the existence of two distinct peaks suggests that the simulation is slightly over-ordered, preventing the nitrate from rotating between oxygen bound to the imidazolium. No shifting of the cation anion pair position is observed over the range of water contents examined. The WAXS data also shows the emergence of a broad, high q (1.90 Å^{-1}) shoulder at higher dilution (Fig. 3D), suggesting the close approach of water molecules at this composition (high dilution). Future X-ray scattering studies that extend the q-range will be carried out to more carefully evaluate the anion cluster structure.

MD simulations reveal that SCN^- prefers to reside out of the plane of the imidazolium ring, positioning itself above or below the aromatic ring with the sulphur atom oriented nearest to the ring (Fig. 1C). Single point EFP calculations determine that this orientation is favoured by 6.1 kcal mol^{-1}. The positioning of SCN^- out of the plane of the imidazolium explains the lack of hydrogen bonding to the ring protons as evidenced experimentally in the absence of resonance shifting in the NMR as a function of water concentration in the binary mixtures. Noted is the disagreement of the thiocyanate location with previously reported MD simulations, which reported that small cyano-substituted anions (such as thiocyanate) solvate imidazolium off-axis (*i.e.*, equatorially), and that larger cyano-anions will solvate above and below the ring.[26] The RDF for single cation to SCN^- as a function of scattering vector, q, was similarly calculated (Fig. 1B). The theoretically predicted location for the ion pair peak is $q = 1.49$ Å^{-1} ($d = 4.22$ Å), a value that is nearly identical to that determined for Cl^-. The WAXS data obtained for a low 4.9% (w/w H_2O) dilution composition yields $d = 4.08$ Å ($q = 1.54$ Å^{-1}) (Fig. 1D). No shifting in the position of this peak is found with increasing the water content to 34.7% (w/w) H_2O (Fig. 1D). Further increasing the water content to 58.9% (w/w) H_2O does show a minor shift of the cation–anion pair peak to $q = 1.58$ Å^{-1} ($d = 3.98$ Å). A shoulder located at higher scattering vector, $q = 1.92$ Å^{-1} ($d = 3.27$ Å), is observed.

The distance here, however, is an average distance from the centroid of the imidazolium ring to the SCN^- position above and/or below the plane of the aromatic ring. Thus, while SCN^- is as close as Cl^- to the cation, the strength of interaction is weaker due to its inability to participate in hydrogen bonding with the ring protons. The theoretical RDF also predicts the presence of a significant secondary solvent shell structure by the appearance of a second correlation peak at $q = 0.90$ Å^{-1} ($d = 7.0$ Å) that is nearly the same magnitude as the first solvent shell peak (ion pair) (Fig. 1B). The secondary shell structure is composed of a water layer residing between the imidazolium cation and the SCN^- (Fig. 1E). This peak is roughly the same magnitude as the peak where the thiocyanate and imidazolium are nearest neighbours, suggesting that there is little preference for the SCN^- to exist as a nearest neighbour to the imidazolium in the first solvation shell. This marks another significant difference between Cl^- ILs where the ratio between the first and second peaks was substantial (*i.e.*, first solvent shell peak larger than the second solvent shell) due to those anions predominantly residing in the first solvent shell. The lack of attraction between the thiocyanate and imidazolium ions and hydrogen bonding is a contributing factor to the observed persistent low viscosity over a wide range of dilutions. The lack of strong ion pair formation also generates poorly (nano) structured mesophases. These findings establish the importance of the IL anion as a critical determinant for establishment of the long-range water structure (network) and nanostructure.

Conclusions

We have performed MD simulations, up to the nanosecond timescale, on $C_{10}mim^+A^-$ (where $A^- = SCN^-, NO_3^-, Cl^-$) ILs using the Effective Fragment Potential (EFP) method and compared the results with experimental data derived from ^{1}H NMR spectroscopy and wide-angle X-ray scattering to evaluate ionic domain structure and interactions (*i.e.*, cation–anion molecular arrangement, hydrogen bonding and competition between ion association and water solvation). The results obtained on the ionic domain were used to interpret observed changes in aqueous IL binary mixture viscosity and nanostructure. The specific findings are as follows. Pairing a strongly coordinating anion, such as Cl^- with $C_{10}mim^+$, generates a robust ion pair attributed to the anion preferentially positioning itself in the plane of the cation aromatic ring and in close proximity to the acidic C-2 proton with secondary association at the C-4 and C-5 protons as predicted by MD trajectories and the calculated RDF. The strong association and proximity between $C_{10}mim^+$ and Cl^- is experimentally verified by WAXS, which gives the average distance between ions in the first solvent shell. The WAXS data further indicated that at high water content (yet preservation of physical gelation) tighter ion aggregates are generated. ^{1}H NMR spectroscopy showed significant C-2 proton up-field shifting with the lessening of the binding between Cl^- and the imidazolium when increased water molecules begin to occupy the space near the C-2 proton. A tight ion pair and strong hydrogen bonding network produces well-ordered nanostructured physical gels adopting a range of symmetries up to very high dilution. Most intriguing is the formation of a high symmetry cubic phase at a high water content of $\sim$43% (w/w), yet with conspicuously less short range order observed in the WAXS. Conversely, at intermediate water content (14% (w/w)) a greatly ordered WAXS pattern indicative of significantly improved short-range ordering yielded a lower symmetry, but well-ordered, 2D hexagonal nanostructure. The observation suggests that an optimized or ideal water content exists for perfecting the IL packing arrangement.

For NO_3^-, MD simulations and RDF calculations indicate that the anion similarly prefers to locate in the imidazolium plane with closest proximity to the acidic C-2 proton and a secondary association at the C-4 and C-5 protons. Nitrate, however, is intermediate in coordinating strength as shown by the longer ion pair distance in the RDF and as confirmed in WAXS. Weakened ion pair strength is also found in the C-2 proton resonances. MD trajectories and RDF predict that NO_3^- is located further from the plane or the imidazolium ring, leading to a lessening of the strength of the ion pair. The theory also indicates that NO_3^- is more susceptible to water insertion, which acts to more readily disrupt ion pair interactions. Thus, NO_3^- is a less coordinating anion, explaining experimental observations of the formation of weak physical gels, a reduction in nanoscale structural ordering, and experimental and theoretical studies confirm that SCN^-

is a non-coordinating anion. MD simulations show that unlike Cl^- and NO_3^-, SCN^- is located out of the plane of the imidazolium ring, sitting above and/or below, a position that inhibits hydrogen bonding with the ring protons. This absence of interaction with imidazolium protons is confirmed by ^{1}H NMR and macroscopically manifests as the lack of significant physical gelation over a wide range of water contents, all factors that lead to poorly formed nanostructures. Furthermore, RDFs calculated on the second solvent shell indicate that water can readily insert into the solvent shell.

In summary, the success of the theory in explaining key experimental data provides strong evidence that the EFP method is a reasonable and robust way to simulate ILs. Importantly, we have begun to observe the emergence of correlation between individual ion pair interactions and long-range (nanoscale) ordering. For example, the results of these studies may be used to estimate an effective head group domain dimension (*e.g.*, imidazolium–anion-associated water) so well established molecular packing parameters[55] can be calculated and used for predicting self-assembled IL architectures. The MD simulations also illustrate the usefulness of having a molecular picture of the physical interactions occurring in these systems. Since new ions of interest can be rapidly parameterized while maintaining a consistent level of accuracy, it is anticipated that these simulation methods will play an important role in the study of unexplored ILs, ultimately providing a means to rapidly screen molecular structures for the *a priori* predication of IL water mixtures for the self-assembly of nanostructures with targeted properties and architectures. While this work only evaluates short range structural ordering between cation, anion and water it lays the foundation for future studies that will consider ensembles of ion pairs.

Acknowledgements

This work was performed, in part, at the Center for Integrated Nanotechnologies (CINT). CINT is funded by the DOE Office of Basic Energy Sciences. LANL is operated by Los Alamos National Security, LLC, for the National Nuclear Security Administration of the U.S. Department of Energy under contract DE-AC52-06NA25396. This research used resources of the Advanced Photon Source, a U.S. Department of Energy (DOE) Office of Science User Facility operated for the DOE Office of Science by Argonne National Laboratory under Contract No. DE-AC02-06CH11357.

References

1 C. Wang, Z. Q. Wang and X. Zhang, *Acc. Chem. Res.*, 2012, **45**, 608–618.
2 E. Busseron, Y. Ruff, E. Moulin and N. Giuseppone, *Nanoscale*, 2013, **5**, 7098–7140.
3 M. A. Firestone, M. L. Dietz, S. Seifert, S. Trasobares, D. J. Miller and N. J. Zaluzec, *Small*, 2005, **1**, 754–760.
4 P. Calandra, D. Caschera, V. T. Liveri and D. Lombardo, *Colloids Surf., A*, 2015, **484**, 164–183.
5 A. J. Olson, Y. H. E. Hu and E. Keinan, *Proc. Natl. Acad. Sci. U. S. A.*, 2007, **104**, 20731–20736.

6 M. A. Firestone, J. A. Dzielawa, P. Zapol, L. A. Curtiss, S. Seifert and M. L. Dietz, *Langmuir*, 2002, **18**, 7258–7260.
7 M. A. Firestone, P. G. Rickert, S. Seifert and M. L. Dietz, *Inorg. Chim. Acta*, 2004, **357**, 3991–3998.
8 D. Batra, D. N. T. Hay and M. A. Firestone, *Chem. Mater.*, 2007, **19**, 4423–4431.
9 S. Lee, G. A. Becht, B. Lee, C. T. Burns and M. A. Firestone, *Adv. Funct. Mater.*, 2010, **20**, 2063–2070.
10 S. M. Brombosz, S. Seifert and M. A. Firestone, *Polymer*, 2014, **55**, 3370–3377.
11 B. Ringstrand, S. Seifert and M. A. Firestone, *J. Polym. Sci., Part B: Polym. Phys.*, 2013, **51**, 1215–1227.
12 D. Batra, S. Seifert and M. A. Firestone, *Macromol. Chem. Phys.*, 2007, **208**, 1416–1427.
13 J. M. Vicent-Luna, D. Dubbeldam, P. Gomez-Alvarez and S. Calero, *ChemPhysChem*, 2016, **17**, 380–386.
14 T. L. Greaves and C. J. Drummond, *Chem. Soc. Rev.*, 2013, **42**, 1096–1120.
15 T. L. Greaves and C. J. Drummond, *Chem. Rev.*, 2015, **115**, 11379–11448.
16 O. Russina, F. Lo Celso, N. V. Plechkova and A. Triolo, *J. Phys. Chem. Lett.*, 2017, **8**, 1197–1204.
17 A. Triolo, O. Russina, H. J. Bleif and E. Di Cola, *J. Phys. Chem. B*, 2007, **111**, 4641–4644.
18 O. Russina, W. Schroer and A. Triolo, *J. Mol. Liq.*, 2015, **210**, 161–163.
19 E. C. Wijaya, T. L. Greaves and C. J. Drummond, *Faraday Discuss.*, 2013, **167**, 191–215.
20 K. Goossens, K. Lava, C. W. Bielawski and K. Binnemans, *Chem. Rev.*, 2016, **116**, 4643–4807.
21 R. Hayes, G. G. Warr and R. Atkin, *Chem. Rev.*, 2015, **115**, 6357–6426.
22 A. Sharma and P. K. Ghorai, *J. Chem. Phys.*, 2016, **144**, 114505–114517.
23 V. L. Martins, B. G. Nicolau, S. M. Urahata, M. C. C. Ribeiro and R. M. Torresi, *J. Phys. Chem. B*, 2013, **117**, 8782–8792.
24 S. V. J. Yuvaraj, R. K. Zhdanov, R. V. Belosludov, V. R. Belosludov, O. S. Subbotin, K. Kanie, K. Funaki, A. Muramatsu, T. Nakamura and Y. Kawazoe, *J. Phys. Chem. B*, 2015, **119**, 12894–12904.
25 S. D. Nickerson, E. M. Nofen, H. B. Chen, M. Ngan, B. Shindel, H. Y. Yu and L. L. Dai, *J. Phys. Chem. B*, 2015, **119**, 8764–8772.
26 K. B. Dhungana, L. F. O. Faria, B. N. Wu, M. Liang, M. C. C. Ribeiro, C. J. Margulis and E. W. Castner, *J. Chem. Phys.*, 2016, **145**, 024503.
27 W. Jiang, Y. T. Wang and G. A. Voth, *J. Phys. Chem. B*, 2007, **111**, 4812–4818.
28 M. S. Gordon, M. A. Freitag, P. Bandyopadhyay, J. H. Jensen, V. Kairys and W. J. Stevens, *J. Phys. Chem. A*, 2001, **105**, 293–307.
29 P. N. Day, J. H. Jensen, M. S. Gordon, S. P. Webb, W. J. Stevens, M. Krauss, D. Garmer, H. Basch and D. Cohen, *J. Chem. Phys.*, 1996, **105**, 1968–1986.
30 N. Kuroki and H. Mori, *Chem. Lett.*, 2016, **45**, 1009–1011.
31 S. Y. S. Tan and E. I. Izgorodina, *J. Chem. Theory Comput.*, 2016, **12**, 2553–2568.
32 P. K. Gurunathan, A. Acharya, D. Ghosh, D. Kosenkov, I. Kaliman, Y. Shao, A. I. Krylov and L. V. Slipchenko, *J. Phys. Chem. B*, 2016, **120**, 6562–6574.
33 *Fundamentals of Analytical Chemistry*, ed. D. A. Skoog and D. A. West, New York, 1976.

34 M. W. Schmidt, K. K. Baldridge, J. A. Boatz, S. T. Elbert, M. S. Gordon, J. H. Jensen, S. Koseki, N. Matsunaga, K. A. Nguyen, S. Su, T. L. Windus, M. Dupuis and J. A. Montgomery, *J. Comput. Chem.*, 1993, **14**, 1347–1363.
35 M. J. Frisch, G. W. Trucks, H. B. Schlegel, G. E. Scuseria, M. A. Robb, J. R. Cheeseman, G. Scalmani, V. Barone, G. A. Petersson, H. Nakatsuji, X. Li, M. Caricato, A. Marenich, J. Bloino, B. G. Janesko, R. Gomperts, B. Mennucci, H. P. Hratchian, J. V. Ortiz, A. F. Izmaylov, J. L. Sonnenberg, D. Williams-Young, F. Ding, F. Lipparini, F. Egidi, J. Goings, B. Peng, A. Petrone, T. Henderson, D. Ranasinghe, V. G. Zakrzewski, J. Gao, N. Rega, G. Zheng, W. Liang, M. Hada, M. Ehara, K. Toyota, R. Fukuda, J. Hasegawa, M. Ishida, T. Nakajima, Y. Honda, O. Kitao, H. Nakai, T. Vreven, K. Throssell, J. A. Montgomery Jr, J. E. Peralta, F. Ogliaro, M. Bearpark, J. J. Heyd, E. Brothers, K. N. Kudin, V. N. Staroverov, T. Keith, R. Kobayashi, J. Normand, K. Raghavachari, A. Rendell, J. C. Burant, S. S. Iyengar, J. Tomasi, M. Cossi, J. M. Millam, M. Klene, C. Adamo, R. Cammi, J. W. Ochterski, R. L. Martin, K. Morokuma, O. Farkas, J. B. Foresman and D. J. Fox, *GAUSSIAN 09, Revision B.01*, Gaussian, Inc, Wallingford, CT, 2010.
36 J. W. Ponder and F. M. Richards, *J. Comput. Chem.*, 1987, **8**, 1016–1024.
37 M. Holz, S. R. Heil and A. Sacco, *Phys. Chem. Chem. Phys.*, 2000, **2**, 4740–4742.
38 I. A. Kaliman and L. V. Slipchenko, *J. Comput. Chem.*, 2013, **34**, 2284–2292.
39 P. C. Hariharan and J. A. Pople, *Theor. Chim. Acta*, 1973, **28**, 213–222.
40 A. F. M. Claudio, L. Swift, J. P. Hallett, T. Welton, J. A. P. Coutinho and M. G. Freire, *Phys. Chem. Chem. Phys.*, 2014, **16**, 6593–6601.
41 D. Xu, Q. W. Yang, B. G. Su, Z. B. Bao, Q. L. Ren and H. B. Xing, *J. Phys. Chem. B*, 2014, **118**, 1071–1079.
42 D. J. Goebbert, E. Garand, T. Wende, R. Bergmann, G. Meijer, K. R. Asmis and D. M. Neumark, *J. Phys. Chem. A*, 2009, **113**, 7584–7592.
43 S. A. Dharaskar, K. L. Wasewar, M. N. Varma and D. Z. Shende, *Environ. Sci. Pollut. Res.*, 2016, **23**, 9284–9294.
44 C. Hardacre, J. D. Holbrey, M. Nieuwenhuyzen and T. G. A. Youngs, *Acc. Chem. Res.*, 2007, **40**, 1146–1155.
45 T. Pott and P. Meleard, *Phys. Chem. Chem. Phys.*, 2009, **11**, 5469–5475.
46 N. A. Bongartz and J. W. Goodby, *Chem. Commun.*, 2010, **46**, 6452–6454.
47 D. Batra, S. Seifert, L. M. Varela, A. C. Y. Liu and M. A. Firestone, *Adv. Funct. Mater.*, 2007, **17**, 1279–1287.
48 G. P. Sorenson, A. K. Schmitt and M. K. Mahanthappa, *Soft Matter*, 2014, **10**, 8229–8235.
49 E. Venugopal, S. K. Bhat, J. J. Vallooran and R. Mezzenga, *Langmuir*, 2011, **27**, 9792–9800.
50 X. B. Zeng, M. Prehm, G. Ungar, C. Tschierske and F. Liu, *Angew. Chem., Int. Ed.*, 2016, **55**, 8324–8327.
51 R. Lungwitz and S. Spange, *New J. Chem.*, 2008, **32**, 392–394.
52 H. K. Kashyap, C. S. Santos, H. V. R. Annapureddy, N. S. Murthy, C. J. Margulis and E. W. Castner, *Faraday Discuss.*, 2012, **154**, 133–143.
53 A. A. Niazi, B. D. Rabideau and A. E. Ismail, *J. Phys. Chem. B*, 2013, **117**, 1378–1388.
54 M. G. Del Popolo and G. A. Voth, *J. Phys. Chem. B*, 2004, **108**, 1744–1752.
55 R. Nagarajan, *Langmuir*, 2002, **18**, 31–38.